Fully Wireless Coherent Distributed Phased Array System for Networked Radar Applications

Jason M. Merlo, *Graduate Student Member, IEEE,* Samuel Wagner, *Member, IEEE,*
John Lancaster, *Member, IEEE,* Jeffrey A. Nanzer, *Senior Member, IEEE*

***Abstract*—In this work we experimentally demonstrate, for the first time, a fully wireless coherent distributed antenna array (CDA) performing distributed transmit and receive beamforming for a down-range sensing application at microwave frequencies without the need for external frequency and time references such as global navigation satellite systems (GNSSs). We build on previous methods utilizing a continuous-wave (CW) two-tone frequency transfer system and a pulsed two-tone time synchronization system to align the distributed platforms in both time and frequency. Coherent transmit and receive beamforming was performed utilizing 100 MHz linear frequency modulation (LFM) waveforms for sensing. Two experiments were performed: one imaging a static scene and one imaging a moving pedestrian holding a corner reflector. The beamforming gain is quantified in the static measurements yielding a median beamforming gain of 2.12 dB and a maximum gain of 2.86 dB (96.5 % coherent beamforming gain).**

***Index Terms*—Automotive radar, distributed antenna arrays, distributed beamforming, networked radar, remote sensing, wireless sensor networks, wireless synchronization.**

I. Introduction

MICROWAVE and millimeter-wave radar systems are an increasingly ubiquitous sensing modality found in devices ranging from automotive platforms' advanced driver assistance systems [1] to Earth remote sensing satellites [2], [3] due to their favorable propagation characteristics, such as relatively low free-space path loss compared to optical wavelengths and ability to propagate through many materials and environmental conditions. However, due to their lower operating frequencies, microwave and millimeter-wave radar systems experience unique challenges with respect to their angular resolution as well as specularity. Angular resolution is important both for resolving closely separated targets at similar range, as well as to mitigate the effects of multipath by isolating direct scatters from reflections off other surfaces in the environment. Specularity can be a challenge, especially at lower frequencies, where objects can create highly angle-dependent scattering profiles, making some objects difficult to detect and localize. Generally, these challenges may be addressed by increasing spectral or spatial diversity [4], [5].

Networked arrays of multi-band antennas can be utilized to satisfy these requirements, however these arrays tend to be large and complex, making them challenging to deploy, especially for applications where size, weight, and power are of principal concern, such as in vehicles. Wirelessly coordinated coherent distributed antenna arrays (CDAs) provide a scalable solution to this challenge [6]. Because individual element nodes may be made small and light, arrays may be scaled over time, and can be reconfigured in real-time to create various array geometries or be removed or added to form smaller or larger arrays, depending on the real-time operational requirements of an imaging task. In addition, due to the mobile nature of wirelessly coordinated CDAs, the array may be physically modulated to achieve time-varying antenna patterns [7] and mitigate the impacts of specularity.

In this work we demonstrate for the first time a wirelessly coordinated coherent distributed sensor array operating at microwave frequencies, without the need for external references such as global navigation satellite systems (GNSSs) during operation, by building on recent advancements in CDA technologies to perform high-accuracy time and frequency synchronization. We demonstrate the system performance in static and dynamic environments, performing real-time coherent beamforming in the broadside direction on transmit and receive.

II. Array Coordination and Calibration

To enable wirelessly coordinated distributed antenna nodes to operate in a coherent manner, stringent alignment of the time, frequency, and phase are required to ensure proper summation of transmitted and received waveforms in a given direction of interest [6]. The transmitted carrier frequency on any distributed radio node may be represented as

$$s^{(n)}(t) = \exp\left\{j2\pi f_c T^{(n)}(t)\right\} + \exp\left(j\phi^{(n)}\right) \qquad (1)$$

where f_c is the desired carrier frequency, $\phi^{(n)}$ is the random initial phase of the local oscillator (LO) at node n and $T^{(n)}(t) = t + \delta^{(n)}(t) = t + \gamma^{(n)}(t) + T_0^{(n)} + w^{(n)}(t)$ is the time of the clock on node n; $\gamma^{(n)}(t)$ is a function representing the integrated clock error at node n, $T_0^{(n)}$ is the initial time offset, and $w^{(n)}(t)$ is a zero-mean noise term due to device noise [8, Ch. 10.1]; $\delta^{(n)}(t)$ is the time bias relative to the global true time t. For simplicity, we will assume that node 0 has the global "true time", thus $\delta^{(0)}(t) \coloneqq 0$.

Frequency syntonization seeks to ensure the clock drift term $\gamma^{(n)}(t)$ is equal across all nodes by disseminating a shared LO amongst all the nodes. The frequency syntonization technique implemented in this work builds on that of [9] and utilizes a continuous-wave (CW) two-tone signal with a tone separation of 10 MHz which is then demodulated by a self-mixing circuit, as seen in Fig. 1. This circuit consists of a bandpass filter on the input to remove out-of-band noise prior to the self-mixing

This article was presented at the IEEE MTT-S International Microwave Symposium (IMS 2024), Washington, DC, USA, June 16–21, 2024.

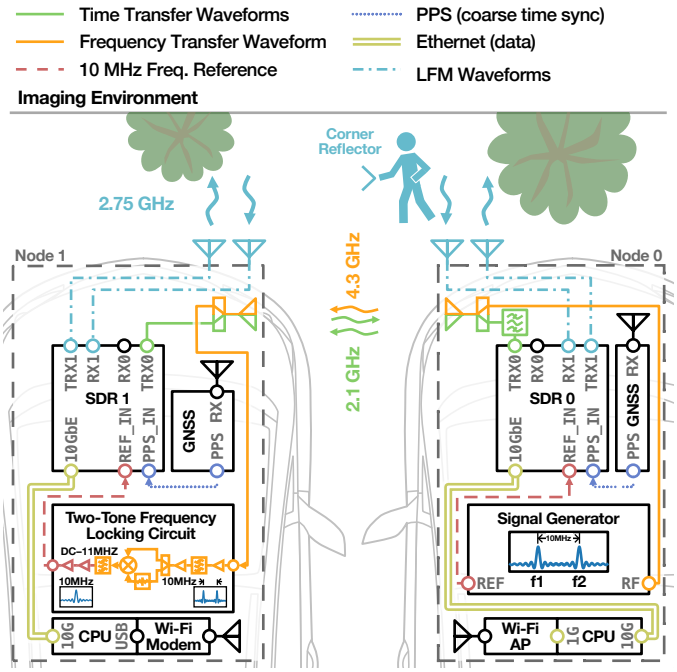

Fig. 1. System schematic with the node carts notionally represented by vehicle outlines. Each node utilized an omni-directional dipole antenna to share time and frequency information; timing information was coordinated using the software-defined radios (SDRs) while frequency was coordinated using a continuous two-tone frequency transfer technique.

stage where the signal is split and mixed with itself producing a beat frequency at the tone separation frequency of 10 MHz and higher terms which are removed via a low-pass filter. The time alignment process seeks to estimate and compensate for the initial time offset $T_0^{(n)}$ and any integrated time errors due to imperfect estimation of $\gamma^{(n)}(t)$. The technique implemented here is based on that demonstrated in [10], which utilizes a high-accuracy two-way time transfer (TWTT) technique to determine the relative clock offsets between nodes as well as the internode distance, which is a critical component for phased array beamforming to determine the appropriate phase weighting at each element to steer a beam in a desired direction. The phase and delay calibration process is performed to compensate for the random initial phase $\phi^{(n)}$ of the LOs and any propagation delay disparity induced by hardware or cable length variations between platforms. To accomplish this, two 160 MHz linear frequency modulation (LFM) waveforms were transmitted to different channels on a Keysight DSOS804A oscilloscope, digitized, transferred to a host computer running GNU Radio and matched filtered to determine the relative delay and phase of the waveforms; several waveforms were collected and the resulting delay $\tau_{\text{cal}}^{(n)}$ and phase $\phi_{\text{cal}}^{(n)}$ estimates were averaged and saved to a database to be used for calibration during operation. After calibration no wires were connected between the systems.

III. Radar Processing

The system consisted of a two element array, with each element having a separate transmit and receive antenna for improved isolation. The system was configured to beamform on transmit and receive, and to steer to the broadside direction. On the transmit side this equated to transmitting a waveform defined by

$$s^{(n)}(t) = \Pi\left(\frac{T_{\text{LFM}}^{(n)}(t)}{\tau_{\text{LFM}}}\right)\exp\left\{j\pi\left[2f_0 T_{\text{LFM}}^{(n)}(t) + \left(\frac{\beta_{\text{LFM}}}{\tau_{\text{LFM}}}\right)\left(T_{\text{LFM}}^{(n)}(t)\right)^2 + \frac{\phi^{(n)} - \phi_{\text{cal}}^{(n)} + \phi_{\text{bf}}^{(n)}}{\pi}\right]\right\} \tag{2}$$

where β_{LFM} is the LFM bandwidth and τ_{LFM} is its duration; $T_{\text{LFM}}^{(n)}(t) = T^{(n)}(t) - \Delta^{(n,0)}(t) - t_{\text{s}}^{(n)}$ where $t_s^{(n)} = t_s + \tau_{\text{LFM}}^{(n)}$ is the start time of the LFM pulse at the nth node; $\tau_{\text{LFM}}^{(n)} = d_{n0}/c\sin\theta_{\text{bf}}$ is its beamforming time delay, $\phi_{\text{bf}}^{(n)} = f_c\tau_{\text{LFM}}^{(n)}$ is its beamforming phase delay, and θ_{bf} is the desired beamforming steering angle. The received waveform was a summation of time-delayed copies of the transmitted waveforms scattered from the scene with L scatterers

$$r^{(n)}(t) = \sum_{m=0}^{N}\sum_{l=0}^{L}\alpha^{(l)}s^{(m)}\left(t - \tau_{\text{d}}^{(l,m,n)}\right) \tag{3}$$

where $\alpha^{(l)}$ is the complex scattering coefficient of the lth scatterer and $\tau_{\text{d}}^{(l,m,n)}$ is propagation delay of the waveform transmitted from the mth transmitter scattering off the lth target received at the nth receiver. The waveform samples were transferred to a central processing location to be summed, then a matched filter was applied to produce the range profile at broadside [11, Ch. 4.2].

IV. Experimental Configuration and Results

The experiment consisted of two distributed antenna nodes containing a transmitter, receiver, and synchronization antenna on each node, shown in the system schematic Fig. 1 and system setup Fig. 2. The transmit and receive antennas were vertically polarized L-Com HG2458-08LP-NF 8-dBi log-periodic antennas located vertically above each other on the antenna masts to reduce coupling. The time-frequency synchronization antennas were commodity dipole antennas. A block of radio frequency absorbing material was placed between the transmit antennas to avoid damage due to direct coupling. The baseline distance between transmit/receive antenna stacks on each mast was 557 mm. To generate the frequency reference, a Keysight E8267D vector signal generator was used on node 0; the 10 MHz reference from the signal generator was used to discipline the LO on software-defined radio (SDR) 0 and the RF output transmitted the 10 MHz two-tone frequency reference at a carrier of 4.3 GHz which was received by the self-mixing circuit on node 1 to discipline the LO on SDR 1. Each node additionally had a GNSS receiver for convenient initial coarse synchronization using a single pulse-per-second (PPS) pulse on each node to align the 30 µs transmit/receive windows; after system initialization the GNSS and PPS signals were no longer used. Each node used an Ettus Research X310 SDR with two UBX-160 daughterboards. The first channel of each SDR was used for time synchronization and internode ranging while the secondary channels were used for radar imaging of the scene. Additionally, each node contained its

TABLE I
BEAMFORMING GAIN AT SCENE FEATURES.

Feature Label	Feature Description	RX0	RX1	BF	BF Gain	
		dB	dB	dB	dB	%–ideal
A	Light post	12.082	11.508	**14.570**	2.765	94.5
B	Corner reflector	13.221	12.240	**13.340**	0.581	57.2
C	Walkway light pedestals	7.057	8.307	**10.172**	2.445	87.8
D	Landscape wall	8.993	8.508	**11.037**	2.279	84.5
E	Archway	**8.119**	5.232	7.572	0.660	58.2
F	West courtyard wall	13.840	7.769	**14.645**	2.857	96.5
G	South courtyard wall	5.121	6.246	**7.174**	1.454	69.9
H	Southwest courtyard corner	3.916	**6.478**	5.516	0.133	51.6
I	South courtyard walkway/bridge	5.323	1.121	**5.544**	1.832	76.2

Boldface numerals denote the highest received power after matched filtering.

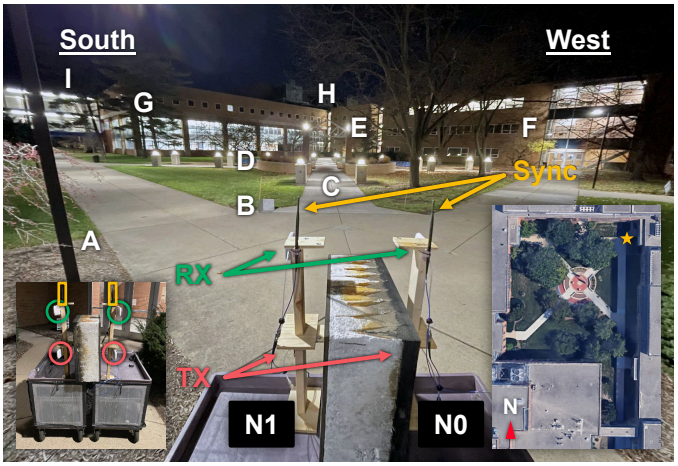

Fig. 2. Courtyard imaging environment and array configuration. Prominent scattering features are labeled which correspond with the labels in Fig. 3. Inset in lower-left corner shows front of system; lower-right corner depicts an aerial view of the courtyard with the star indicating the radar array (Imagery ©2023 Google, map data ©2023).

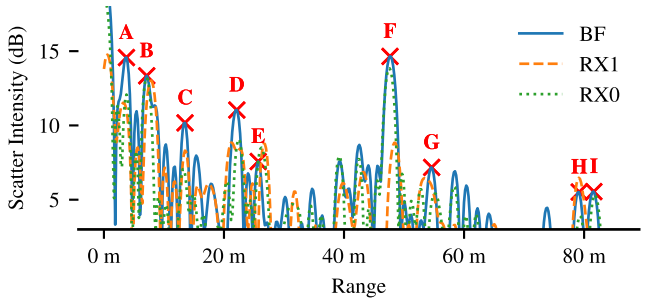

Fig. 3. Downrange measurements of the static courtyard environment. The solid line indicates the signal after coherent summation of both signals on receive and matched filtering; dotted and dashed lines indicate the measured signal at receivers 0 and 1, respectively, after matched filtering. In all cases the transmitted signal was beamformed towards broadside. The letters above peaks indicate selected scene features which correspond with labels in Fig. 2.

own computer using an Intel i7-8700 with 16 GB of memory running Ubuntu 22.04 and GNU Radio to perform the time synchronization process, sharing timestamp information using TCP/IP over Wi-Fi at 5.825 GHz. The received samples were also transferred via TCP/IP over Wi-Fi to node 0 for final processing, image formation, and datalogging.

The down-range imaging experiment was performed in an enclosed courtyard shown in Fig. 2 with prominent features labeled A–I. Two experiments were performed: imaging a static scene, and imaging a dynamic scene. In the dynamic scene, the corner reflector (B) was carried to the center of the courtyard by a pedestrian and then returned to the original location. In the static scene experiment, the system was turned on and allowed to run and synchronize; after several minutes, the static scene image was taken. Statistics of the system synchronization in the 20 s around the time of the static scene capture were computed and indicated a time synchronization standard deviation of 53.7 ps with a maximum deviation of 100.1 ps. The matched filter results from the individual antennas on nodes 0 and 1 as well as the matched filter after receive-side beamforming are shown in Fig. 3 with red labels corresponding to those shown in Fig. 2 and Table I. Table I displays the received power after matched filtering in decibels for RX0, RX1, and after beamforming (denoted BF); the sixth column indicates the gain in decibels relative to the average of RX1 and RX2 while the final column indicates the gain as a percentage of the ideal summation of RX0 and RX1. The gain is shown to be as high as 96.5 % for some scatterers, however, some scatterers show significantly lower results; this is likely due to specularity of some objects observed at each node as well as multipath scattering in the environment causing incoherent summation of signals due to differing path lengths between direct and indirect scatters. However, in all cases the summed signal is an improvement over the average of the individual responses; moreover, the beamformed signal was the highest response in most of the prominent scatterers. Finally, statistics were computed for the beamforming gain across all peaks in the scene yielding a mean beamforming gain of 1.89 dB (77.3 % of the theoretical ideal value), a median gain of 2.12 dB (81.5 %-ideal), and a maximum gain of 2.86 dB (96.5 %-ideal).

The dynamic scene was captured immediately following the static scene while the system was still running. The downrange scatter intensity vs. time are shown in the waterfall plot in Fig. 4 (top) with the magnitude of the time synchroniza-

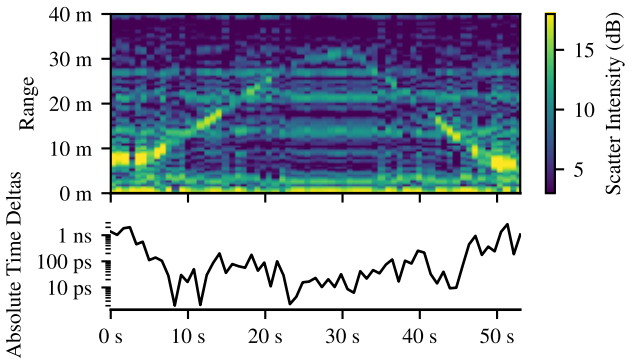

Fig. 4. (Top) Downrange measurements of a pedestrian carrying a corner reflector to the center of the courtyard and returning. (Bottom) Absolute time update deltas for clock compensation during the dynamic recording. Measurements were collected at ∼1 Hz.

tion corrections shown below. Between each radar snapshot a time resynchronization exchanged occurred. A triangular shaped yellow line can be clearly seen in the waterfall plot tracing out the range–time profile the pedestrian took during the experiment. The time synchronization correction standard deviation was 588 ps, significantly larger than the static scene. This is believed to be due to the synchronization epoch duration being on the order of ∼200 ms due to limitations of its current implementation; because the assumption of the TWTT protocol is that the wireless channel is reciprocal, i.e. quasi-static, during the epoch is likely violated when there are dynamic scatterers, the synchronization stability decreases significantly when the pedestrian is near the system; however, once the pedestrian exceeds 20 m the system returns to sub-100 ps level of synchronization.

V. Conclusion

In this paper we demonstrate, a CDA performing beamforming and down-range imaging operations without the need for auxiliary time or frequency reference sources. We show that the system is capable of achieving a median coherent beamforming gain of 2.12 dB (81.5 %-ideal), and a maximum gain of 2.86 dB (96.5 %-ideal) for a static scene, and demonstrate qualitatively system performance tracking a pedestrian in a dynamic scene.

Acknowledgment

This work was supported under the auspices of the U.S. Department of Energy by Lawrence Livermore National Laboratory under Contract DEAC52-07NA27344, by the LLNL-LDRD Program under Project No. 22-ER-035. Distributed Statement A. Approved for public release: distribution unlimited. Release number: LLNL-JRNL-857989.

References

[1] C. Waldschmidt, J. Hasch, and W. Menzel, "Automotive radar—from first efforts to future systems," *IEEE Journal of Microwaves*, vol. 1, no. 1, pp. 135–148, 2021.

[2] G. Krieger, A. Moreira, H. Fiedler, I. Hajnsek, M. Werner, M. Younis, and M. Zink, "Tandem-x: A satellite formation for high-resolution sar interferometry," *IEEE Transactions on Geoscience and Remote Sensing*, vol. 45, no. 11, pp. 3317–3341, 2007.

[3] R. Werninghaus and S. Buckreuss, "The terrasar-x mission and system design," *IEEE Transactions on Geoscience and Remote Sensing*, vol. 48, no. 2, pp. 606–614, 2010.

[4] K. Abratkiewicz, P. J. Samczyński, R. Rytel-Andrianik, and Z. Gajo, "Multipath interference removal in receivers of linear frequency modulated radar pulses," *IEEE Sensors Journal*, vol. 21, no. 17, pp. 19 000–19 012, 2021.

[5] J. Liang and Q. Liang, "Design and analysis of distributed radar sensor networks," *IEEE Transactions on Parallel and Distributed Systems*, vol. 22, no. 11, pp. 1926–1933, 2011.

[6] J. A. Nanzer, S. R. Mghabghab, S. M. Ellison, and A. Schlegel, "Distributed phased arrays: Challenges and recent advances," *IEEE Trans. Microw. Theory Techn.*, vol. 69, no. 11, pp. 4893–4907, 2021.

[7] S. M. Ellison, J. M. Merlo, and J. A. Nanzer, "Distributed antenna array dynamics for secure wireless communication," *IEEE Transactions on Antennas and Propagation*, vol. 70, no. 4, pp. 2740–2749, 2022.

[8] D. Pozar, *Microwave Engineering*, 3rd ed. John Wiley & Sons, Inc., 2005.

[9] S. R. Mghabghab and J. A. Nanzer, "Open-loop distributed beamforming using wireless frequency synchronization," *IEEE Trans. Microw. Theory Techn.*, vol. 69, no. 1, pp. 896–905, 2021.

[10] J. M. Merlo, S. R. Mghabghab, and J. A. Nanzer, "Wireless picosecond time synchronization for distributed antenna arrays," *IEEE Transactions on Microwave Theory and Techniques*, pp. 1–12, 2022.

[11] M. Richards, *Fundamentals of Radar Signal Processing, Second Edition*. McGraw-Hill Education, 2014.